SCIENTIFIC REP🞄RTS

OPEN

Heterogeneous TiO_2@Nb_2O_5 composite as a high-performance anode for lithium-ion batteries

Yubin Liu[1,2], Liwei Lin[2], Weifeng Zhang[1,2] & Mingdeng Wei[1,2]

Heterogeneous TiO_2@Nb_2O_5 composites, in which TiO_2 nanoparticles were evenly embedded on ultrathin Nb_2O_5 nanosheets, were used as anode materials for LIBs and demonstrated high capacities and excellent rate capability. For instance, this material displayed large capacities of 166.3 and 129.1 mA h g^{-1} at current densities of 1 A g^{-1} after 100 cycles and 5 A g^{-1} after 300 cycles, respectively.

To meet the demand for large application of lithium-ion batteries (LIBs) in the field of hybrid electric vehicles and electric vehicles, development of electrode materials with high capacity and superior rate capability is urgent[1–3]. Over the past few decades, TiO_2 have been considered as an alternative anode material for LIBs because of chemical stability, safety, environmental friendliness as well as a negligible volume change in Li-ion intercalation[4–8]. In particular, nanostructured TiO_2, with short electron/ion diffusion distance and high surface area, exhibit enhanced lithium-ion intercalation properties[9–12]. Notably, ultrafine TiO_2 with several nanometers can reveal pseudocapacitance storage process as well as lithium intercalation process, resulting in an increase of the total amount of Li storage and improved rate capability[13, 14]. However, nanostructured TiO_2 are prone to suffer from server aggregation which dramatically diminishes its rate performances and cycling stabilities.

Dispersion of nanosized TiO_2 onto other materials with a large surface area is one of the strategies to overcome the above drawback of TiO_2, because they can efficiently inhibit aggregation of TiO_2. Conventionally, carbonaceous materials have been considered as excellent supports for TiO_2 because of its excellent electronic conductivity. Thus, TiO_2@carbon composite nanofibers[15], TiO_2/carbon nanotubes[16] and TiO_2-mesoporous carbon nanocomposites[17] have been explored for lithium storage. Among these carbonaceous materials, the graphene with a two-dimensional structure appears particularly promising to improve the electrochemical performance of TiO_2 composite materials and served as a support for nanostructured TiO_2 due to its superior electrical conductivity, large surface area and excellent structural flexibility[18–24]. For examples, Wang *et al.* used anionic sulfate surfactants to synthesize TiO_2-graphene hybrid, which showed improved electrochemical performance[25]. Zhang *et al.* reported a simple one-step hydrothermal method toward *in situ* growth of mesoporous TiO_2 on 3D-graphene aerogels, which displayed a reversible capacity of 99 mA h g^{-1} at a high rate of 5000 mA g^{-1} [26]. Nevertheless, a homogenous dispersion of TiO_2 nanoparticles onto graphene remains a challenge because of intrinsic incompatibility of graphene with inorganic components[18, 27–29]. On the other hand, graphene barely contribute to the capacity in operating potential windows of TiO_2 (in the range of 1.0 between 3.0 V vs. Li$^+$/Li). Therefore, it is highly desirable to develop other materials as supports for nanosized TiO_2 deposition. Kim *et al.* reported that TiO_2 nanoparticles were uniformly assembled onto high-conductivity indium tin oxide nanowire arrays, which exhibited a large capacity of more than 200 mA h g^{-1} at a 60 C rate[30]. Gu *et al.* reported that Ag nanowires/mesoporous TiO_2 delivered a reversible capacity of ~160 mA h g^{-1} after 230 cycles at a current density of 1 C[31].

In the present work, heterogeneous TiO_2@Nb_2O_5 composites, in which TiO_2 nanoparticles were evenly embedded on ultrathin Nb_2O_5 nanosheets, were successfully synthesized for the first time. Furthermore, this composite was used as an anode for LIBs and delivered high reversible capacities and superior rate capability.

Results

The morphology and structure of TiO_2@Nb_2O_5 composites are firstly characterized by SEM and TEM, respectively. A SEM image in Fig. 1a gives us a full view of the obtained TiO_2@Nb_2O_5 composites, in which uniform sheet-like morphology with thin thickness can be observed. Unlike pure Nb_2O_5 nanosheets (Figure S1), the surface of TiO_2@Nb_2O_5 composites appeared rough (Fig. 1b). It is noteworthy that the thickness of these nanosheets

[1]State Key Laboratory of Photocatalysis on Energy and Environment, Fuzhou University, Fuzhou, Fujian, 350002, China. [2]Institute of Advanced Energy Materials, Fuzhou University, Fuzhou, Fujian, 350002, China. Correspondence and requests for materials should be addressed to M.W. (email: wei-mingdeng@fzu.edu.cn)
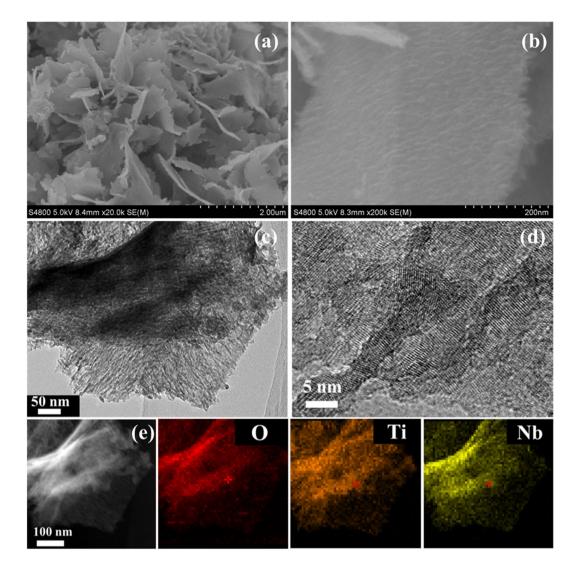
Figure 1. (**a,b**) SEM image, (**c,d**) TEM images and (**e**) STEM image and elemental mappings of TiO_2@Nb_2O_5 composites.

was larger than that of pure Nb_2O_5 nanosheets. The surface difference of TiO_2@Nb_2O_5 composites and Nb_2O_5 nanosheets indicates that TiO_2 nanoparticles were embedded on Nb_2O_5 nanosheets. Apart from the uniform TiO_2@Nb_2O_5 composites, single TiO_2 nanoparticles are not observed. TEM images in Fig. 1c shows that the whole surface of Nb_2O_5 nanosheets was covered with TiO_2 nanoparticles, and further confirms that TiO_2@Nb_2O_5 heterogeneous structure can be formed. In a HRTEM image of TiO_2@Nb_2O_5 composites in Fig. 1d, it can be found that the size of TiO_2 nanoparticles was about 5 nm, which is smaller than that of pure TiO_2 nanoparticles (Figure S1f). To investigate the chemical composition of the TiO_2@Nb_2O_5 composites, EDX analysis was carried out and the result is depicted in Figure S3. Strong O, Ti and Nb signals can be observed and ICP-OES results (Table S1) showed that the atomic ratio of Nb to Ti was 0.44. At the same time, STEM image and the corresponding elemental mappings O, Ti and Nb were performed to investigate the distribution of TiO_2 nanoparticles in the Nb_2O_5 nanosheets. As shown in Fig. 1e, TiO_2 nanoparticles were evenly embedded on the surface of Nb_2O_5 nanosheets.

AFM measurement was performanced to determine the thicknesses of Nb_2O_5 nanosheets and TiO_2@Nb_2O_5 composites. As shown in Fig. 2, the thicknesses of Nb_2O_5 nanosheets and TiO_2@Nb_2O_5 composites were about 4.5 and 16 nm, respectively, further indicating that the size of TiO_2 nanoparticles was about 6 nm. On the other hand, it can be clearly found that the surface of Nb_2O_5 nanosheets appeared smooth, while the surface of TiO_2@Nb_2O_5 composites was rough. The AFM results were in good agreement with SEM and TEM results.

Figure 3 shows the XRD patterns of TiO_2@Nb_2O_5 composites. The diffraction peaks can be indexed to the mixed of monoclinic Nb_2O_5 (JCPDS 43-1042) and anatase TiO_2 (JCPDS 21-1272). Furthermore, Raman spectra of TiO_2 nanoparticles, Nb_2O_5 nanosheets and TiO_2@Nb_2O_5 composites were also recorded and the results are presented in Figure S2. Raman spectrum of TiO_2@Nb_2O_5 composites exhibited the characteristic peaks of anatase TiO_2 and weak peaks of Nb_2O_5, which is consistent with the XRD result.
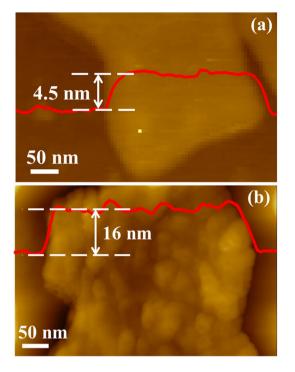
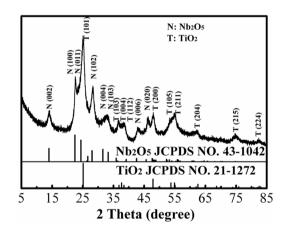**Figure 2.** AFM images of (**a**) Nb_2O_5 nanosheets and (**b**) $TiO_2@Nb_2O_5$ composites.

Figure 3. XRD patterns of $TiO_2@Nb_2O_5$ composites.

To investigate the Brunauer-Emmett-Teller (BET) surface area and porous structure of $TiO_2@Nb_2O_5$ composites, N_2 adsorption-desorption isotherms of this material was measured and the results are depicted in Fig. 4. Similar to Nb_2O_5 nanosheets (Figure S5b), $TiO_2@Nb_2O_5$ composites exhibited a type-IV isotherm with a type-H3 hysteresis loop, indicating that $TiO_2@Nb_2O_5$ composites maintain sheet-like morphology. However, it is noteworthy that the range of hysteresis loop for $TiO_2@Nb_2O_5$ composites is larger than that of Nb_2O_5 nanosheets (Figure S5b), which can be ascribed to the slight aggregation of TiO_2 nanoparticles on the surface of Nb_2O_5 nanosheets. The BET surface area of TiO_2 nanoparticles, Nb_2O_5 nanosheets and $TiO_2@Nb_2O_5$ composites are 85.6, 99.8 and 134.6 $m^2 g^{-1}$, respectively. Homogeneous dispersion of TiO_2 nanoparticles onto Nb_2O_5 nanosheets increased the thickness of these composites and inhibited aggregation of nanosheets. On the other hand, the structure of TiO_2 nanoparticles embedded on nanosheets prevents the undesirable aggregation. Therefore, $TiO_2@Nb_2O_5$ composites show an inconspicuous BJH pore size (Fig. 4b), which is different to that of Nb_2O_5 nanosheets (inset in Figure S5b) or TiO_2 nanoparticles (inset in Figure S5a).

Figure 5a shows CV curves of $TiO_2@Nb_2O_5$ composites at a scan rate of $0.5 \, mV \, s^{-1}$ in range of 1.0–3.0 V. All cathodic and anodic peaks can be ascribed to the mixed of monoclinic Nb_2O_5 and anatase TiO_2. Several broad cathodic and anodic peaks in the potential range of 1.1–2.2 V can be observed, which are similar to those of other Nb_2O_5[32–36]. In addition, $TiO_2@Nb_2O_5$ composites also shows representative CV curves of anatase TiO_2, in which two well-defined cathodic and anodic peaks at ~1.7 and 2.0 V can be clearly observed, respectively. The electrochemical performance of $TiO_2@Nb_2O_5$ composites was evaluated by galvanostatic charge-discharge cycling at
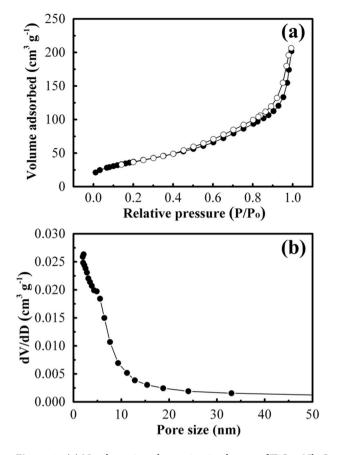
Figure 4. (**a**) N_2 adsorption-desorption isotherms of $TiO_2@Nb_2O_5$ composites and (**b**) the corresponding pore size distributions calculated using the BJH method.

different current densities. Fig. 5b shows the charge-discharge voltage profiles of $TiO_2@Nb_2O_5$ composites electrode in the 1st and 2nd cycle at a current density of $1\,A\,g^{-1}$. Interestingly, $TiO_2@Nb_2O_5$ composites also displayed sloping charge-discharge profiles, which was very similar to that of Nb_2O_5 nanosheets (Figure S7a). Namely, the two typical voltage plateaus of TiO_2 cannot be observed in charge-discharge voltage profiles of $TiO_2@Nb_2O_5$ composites. This might be ascribed to the effect of particle size of TiO_2 on the galvanostatic charge-discharge process[13]. Comparison with Nb_2O_5 nanosheets (Figure S7a) or TiO_2 nanoparticles (Figure S7b), $TiO_2@Nb_2O_5$ composites delivered a superior initial discharge and charge capacities of 216.8 and $174.3\,mA\,h\,g^{-1}$ with a high Coulombic efficiency of 80.4%. The first irreversible capacity loss can be attributed to some irreversible side reactions inside the electrode materials[37].

As shown in Fig. 6, $TiO_2@Nb_2O_5$ composites exhibited high reversible capacities of $166.3\,mA\,h\,g^{-1}$ after 100 cycles at $1\,A\,g^{-1}$ and $129.1\,mA\,h\,g^{-1}$ after 300 cycles at $5\,A\,g^{-1}$, respectively. In addition, the Coulombic efficiency rapidly increased to nearly 100% after first several cycles. On the other hand, the rate capability of TiO_2 nanoparticles, Nb_2O_5 nanosheets and $TiO_2@Nb_2O_5$ composites were evaluated and the results were shown in Fig. 6c and Figure S9. It is clear that $TiO_2@Nb_2O_5$ composites exhibited a significantly improved rate capability over TiO_2 nanoparticles or Nb_2O_5 nanosheets. The capacities of 194.9, 184.8, 173.2, 161.8, 149.3 and $136.0\,mA\,h\,g^{-1}$ were achieved for $TiO_2@Nb_2O_5$ composites at 0.1, 0.2, 0.5, 1, 2 and $5\,A\,g^{-1}$, respectively. When the current density was back to $0.2\,A\,g^{-1}$, the capacity of $177.1\,mA\,h\,g^{-1}$ was obtained after 50 cycles.

It is well known that Nb_2O_5 is a kind of pseudocapacitative materials[32–34]. At the same time, TiO_2 with small size also shows a pseudocapacitative behavior[12, 13]. To further authenticate the pseudocapacitive feature in $TiO_2@Nb_2O_5$ composites, CV curves with different scan rates in cathodic process were presented in Fig. 7a. The total stored charge can be separated into three componets: the Faradaic contribution from the Li^+ ion intercalation process, pseudocapacitance and nonFaradaic contribution from the double layer effect. The differnet storage mechanisms can be determined by investigating the change of the peak current (i) with the scan rate (ν) according to the following equation 1[13]:

$$i = a\nu^b \tag{1}$$

where both a and b are adjustable parameters. When the b value is about 0.5, it implies that Li^+ ion intercalation process is a dominant process; while the b value is close to 1, it indicates that stored charge mostly come from the surface capacitive effect. As shown in Fig. 7b, the fitting b values at the voltages of 1.3, 1.5, 1.9, 2.1 and 2.3 V were 0.90, 0.87, 0.85, 0.92 and 0.83, respectively, which are very close to 1 and suggest that the lithium storage process
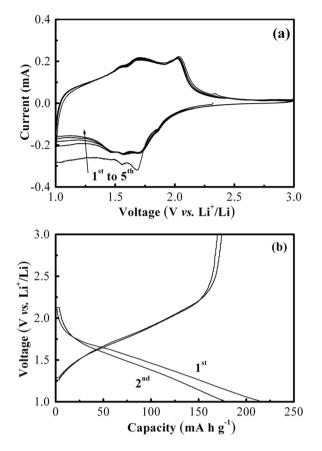
Figure 5. The electrochemical properties of $TiO_2@Nb_2O_5$ composites: (**a**) CV curves with a scan rate of $0.5\,mV\,s^{-1}$ and (**b**) charge-discharge profiles at a current density of $1\,A\,g^{-1}$.

is mostly dominated by the pseudocapacitative contributions. It's worth noting that the fitting b value of 0.75 at the voltage of 1.7 V was relatively low, which implied the current comes primarily from Li^+ ion intercalation and pseudocapacitative process. The high performance of $TiO_2@Nb_2O_5$ composites would be mainly related to this pseudocapacitive storage process.
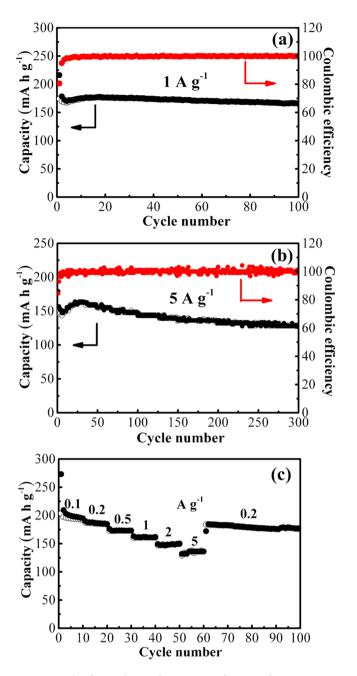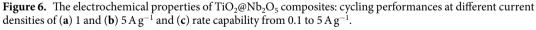
Discussion

In the present work, heterogeneous $TiO_2@Nb_2O_5$ composites show high capacities at high-rate over TiO_2@carbonaceous materials, as listed in Table 1. The excellent performance of $TiO_2@Nb_2O_5$ composites can be attributed to the synergistic effects of nanostructured TiO_2 and Nb_2O_5 as following: (i) $TiO_2@Nb_2O_5$ composites with a surface area as large as $134.6\,m^2\,g^{-1}$ can enhance the contact between the electrolyte and the electrode; (ii) nanosheet-like Nb_2O_5 as a support can buffer aggregation of TiO_2 nanoparticles, and TiO_2 nanoparticles embedded on Nb_2O_5 nanosheets offer a short diffusion distance and more surface storage sites for Li^+ ions, thus promoting fast and reversible lithium intercalation/deintercalation into/from electrode and enhanced capacity; (iii) pseudocapacitive behavior of Nb_2O_5 nanosheets can deliver a high reversible capacity at high current densities[32, 33, 38].

In summary, a two-step synthetic route was firstly developed for synthesizing heterogeneous $TiO_2@Nb_2O_5$ composites, in which TiO_2 nanoparticles were evenly embedded on the surface of ultrathin Nb_2O_5 nanosheets. When used as anode material for lithium-ion batteries, it showed high capacities and superior rate capability in comparison to pure TiO_2 nanoparticles or Nb_2O_5 nanosheets due to their synergistic effects as following: The composite with a large surface area can enhance the contact between the active material and the electrolyte; the aggregation of TiO_2 nanoparticles can be buffered on the surface of Nb_2O_5 nanosheets; TiO_2 nanoparticles embedded on Nb_2O_5 nanosheets offer a short diffusion distance and more surface storage sites for Li^+ ions; pseudocapacitive behavior of Nb_2O_5 can deliver a high reversible capacity at high current densities. Therefore, such heterogeneous nanostructure has a great potential application in field of photocatalysis, Li/Na-ion batteries and supercapacitors.

Methods

Synthesis of Nb_2O_5 nanosheets, TiO_2 nanoparticles and $TiO_2@Nb_2O_5$ composites.   6 g of urea was dissolved in 30 mL of ethylene glycol (EG). After stirring for 10 min, 0.25 g of niobium (V) oxalate hydrate was added into above solution under stirring, and then the resulting solution was transferred into Teflon coated stainless steel with a capacity of 50 mL. The autoclave was kept at 200 °C for 2 days and then naturally cooled to room temperature. The white product was harvested via centrifugation, washed thoroughly with ethanol for

Figure 6. The electrochemical properties of $TiO_2@Nb_2O_5$ composites: cycling performances at different current densities of (**a**) 1 and (**b**) $5\,A\,g^{-1}$ and (**c**) rate capability from 0.1 to $5\,A\,g^{-1}$.

several times and dried in an oven at 70 °C overnight. To obtain Nb_2O_5 nanosheets, the above white product was annealed at 500 °C in air for 2 h with a heating rate of $2\,°C\,min^{-1}$.

For the synthesis of $TiO_2@Nb_2O_5$ composites, the 50 mg of as-prepared Nb_2O_5 nanosheets were added into a 50 mL Teflon container with pre-filled with 30 mL ethylene glycol (EG) under stirring. After stirring for 3 h, 0.2 mL of titanium isopropoxide (TTIP) was dropwise added into the above suspension. After stirring for another 3 h, 4.0 g of urea was dissolved in above solution under stirring to form a white solution which was transferred into Teflon coated stainless steel. The autoclave was kept at 180 °C for 24 h and naturally cooled to room temperature. The white product was separated by centrifugation, washed with ethanol for several times and dried in an oven at 70 °C overnight. The resulting product was annealed at 400 °C in air for 2 h with a heating rate of $2\,°C\,min^{-1}$ and $TiO_2@Nb_2O_5$ composites were obtained.

TiO_2 nanoparticles were synthesized following the same procedure of $TiO_2@Nb_2O_5$ composites except for the addition of Nb_2O_5 nanosheets.

Characterizations. X-ray diffraction (XRD) patterns of products were recorded on a Rigaku Ultima IV X-ray diffractomator by using CuKα radiation. Scanning electron microscopy (SEM, Hitachi S4800 instrument)
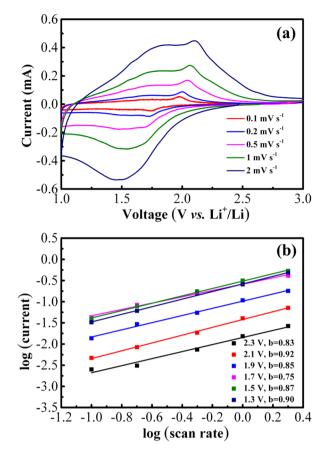
Figure 7. (**a**) CV curves of $TiO_2@Nb_2O_5$ composites with different scan rates and (**b**) their corresponding log (current) *vs* log (scan rate) fitting lines.

Composite TiO_2	Discharge capacity (mA h g^{-1})	Current density (mA g^{-1})	References
$TiO_2@Nb_2O_5$	166.3 (after 100 cycles)	1000	present work
	129.1 (after 300 cycles)	5000	
$TiO_2@$carbon nanotube	203 (after 100 cycles)	100	16
	101 (after 100 cycles)	4000	
TiO_2 nanosheets@graphene	161 (after 120 cycles)	170	19
	119 (after 120 cycles)	1700	
TiO_2 nanoparticles@graphene	175 (after 100 cycles)	100	20
	125 (after 100 cycles)	2000	
TiO_2 quantum-dot@graphene	190 (after 100 cycles)	168	24
	145 (after 100 cycles)	1680	
$TiO_2@$mesoporous carbon	133.9 (after 100 cycles)	500	39
	81.2 (after 100 cycles)	3000	

Table 1. Comparison of the cycling performance of $TiO_2@Nb_2O_5$ with some representative $TiO_2@$ carbonaceous materials as an anode for LIBs.

and transmission electron microscopy (TEM, FEI F20 S-TWIN instrument) were applied for the determination of products morphology and composition. The STEM mapping is TEM-based STEM and a voltage of 200 KV was used for the mapping. Atomic Force Microscope (AFM, Agilent Technologies) was used to determine the thickness and morphology of products. The Raman spectra were recorded in a Renishaw inVai Raman microscope with a 532 nm laser. N_2 adsorption-desorption was performed on a Micromeritics ASAP 2020 instrument (Micromeritics, Norcross, GA, USA). BET surface area of the obtained samples were measure by nitrogen adsorption and desorption isotherms at 77 K after the samples were degassed under vacuum at 220 °C for 6 h. The pore size distributions of the samples were analyzed by using the BJH methods. The contents of Nb_2O_5 and TiO_2 in the prepared composites were determined by PerkinElmer Optima 8000 inductively coupled plasma optical emission spectrometry (ICP-OES).

Electrochemical measurements.   The electrochemical performance of all products was performed using 2025-type coin cells with two-electrodes. First, the resulting products were admixed with polyvinylidene fluoride (PVDF) binder and acetylene black carbon in a weight ratio of 7:2:1 to form a slurry which was coated on copper foil circular flakes and dried at 110 °C in a vacuum overnight. Copper foils coated active materials were used as working electrodes and Lithium foils were used as the counter electrodes. The electrolyte was 1 M $LiPF_6$ in a 1:1:1 (volume ratio) mixture of ethylene carbonate (EC), ethylene methyl carbonate (EMC) and dimethyl carbonate (DMC). Celgard2400 (America) microporous polypropylene membrane was used as the separator. Cell assembly was carried out in a glove box filled with highly pure argon gas (O_2 and H_2O levels <1 ppm). Cyclic voltammetry (CV) and charge-discharge tests of all electrodes were performed using an electrochemical workstation (CHI 600 C) and Land automatic batteries tester (Land, CT 2001A, Wuhan, China), respectively. The specific capacities of $TiO_2@Nb_2O_5$ were calculated based on the weight of the composites.

References

1. Tarascon, J. M. & Armand, M. Issues and challenges facing rechargeable lithium batteries. *Nature* **414**, 359–367 (2001).
2. Goodenough, J. B. & Kim, Y. Challenges for rechargeable Li batteries. *Chem. Mater.* **22**, 587–603 (2001).
3. Armand, M. & Tarascon, J. M. Building better batteries. *Nature* **451**, 652–657 (2008).
4. Zhu, G. N., Wang, Y. G. & Xia, Y. Y. Ti-based compounds as anode materials for Li-ion batteries. *Energy Environ. Sci.* **5**, 6652–6667 (2012).
5. Huang, S. Y., Kavan, L., Exnar, I. & Gratzel, M. Rocking chair lithium battery based on nanocrystalline TiO_2 (anatase). *J. Electrochem. Soc.* **142**, L142–L144 (1995).
6. Su, X. *et al.* Advanced titania nanostructures and composites for lithium ion battery. *J. Mater. Sci.* **47**, 2519–2534 (2012).
7. Wu, Q. *et al.* Ultrathin anatase TiO_2 nanosheets embedded with TiO_2-B nanodomains for lithium-ion storage: capacity enhancement by phase boundaries. *Adv. Energy Mater.* **5**, 1401756 (2015).
8. Zhang, R. Y., Elzatahry, A. A., Al-Deyab, S. S. & Zhao, D. Y. Mesoporous titania: From synthesis to application. *Nano Today* **7**, 344–366 (2012).
9. Hu, Y. S., Kienle, L., Guo, Y. G. & Maier, J. High lithium electroactivity of nanometer-sized rutile TiO_2. *Adv. Mater.* **18**, 1421 (2006).
10. Arico, A. S., Bruce, P., Scrosati, B., Tarascon, J. M. & Van Schalkwijk, W. Nanostructured materials for advanced energy conversion and storage devices. *Nat Mater.* **4**, 366–377 (2005).
11. Bruce, P. G., Scrosati, B. & Tarascon, J. M. Nanomaterials for rechargeable lithium batteries. *Angew. Chem. Int. Ed.* **47**, 2930–2946 (2008).
12. Jiang, C. H. *et al.* Particle size dependence of the lithium storage capability and high rate performance of nanocrystalline anatase TiO_2 electrode. *J. Power Sources* **166**, 239–243 (2007).
13. Wang, J., Polleux, J., Lim, J. & Dunn, B. Pseudocapacitive contributions to electrochemical energy storage in TiO_2 (anatase) nanoparticles. *J. Phys. Chem. C* **111**, 14925–14931 (2007).
14. Zhu, K., Wang, Q., Kim, J. H., Pesaran, A. A. & Frank, A. J. Pseudocapacitive lithium-ion storage in oriented anatase TiO_2 nanotube arrays. *J. Phys. Chem. C* **116**, 11895–11899 (2012).
15. Yang, Z. X. *et al.* Synthesis of uniform $TiO_2@carbon$ composite nanofibers as anode for lithium ion batteries with enhanced electrochemical performance. *J. Mater. Chem.* **22**, 5848–5854 (2012).
16. Wang, J., Ran, R., Tade, M. O. & Shao, Z. Self-assembled mesoporous TiO_2/carbon nanotube composite with a three-dimensional conducting nanonetwork as a high-rate anode material for lithium-ion battery. *J. Power Sources* **254**, 18–28 (2014).
17. Chang, P. Y., Huang, C. H. & Doong, R. A. Ordered mesoporous carbon-TiO_2 materials for improved electrochemical performance of lithium ion battery. *Carbon* **50**, 4259–4268 (2012).
18. Yang, S., Feng, X. & Müllen, K. Sandwich-like, graphene-based titania nanosheets with high surface area for fast lithium storage. *Adv. Mater.* **23**, 3575–3579 (2011).
19. Ding, S. *et al.* Graphene-supported anatase TiO_2 nanosheets for fast lithium storage. *Chem. Commun.* **47**, 5780–5782 (2011).
20. Li, W. *et al.* Sol-gel design strategy for ultradispersed TiO_2 nanoparticles on graphene for high-performance lithium ion batteries. *J. Am. Chem. Soc.* **135**, 18300–18303 (2013).
21. Li, N. *et al.* Battery performance and photocatalytic activity of mesoporous anatase TiO_2 nanospheres/graphene composites by template-free self-assembly. *Adv. Funct. Mater.* **21**, 1717–1722 (2011).
22. Xin, X., Zhou, X., Wu, J., Yao, X. & Liu, Z. Scalable synthesis of TiO_2/graphene nanostructured composite with high-rate performance for lithium ion batteries. *ACS Nano* **6**, 11035–11043 (2012).
23. Zhang, X. *et al.* Electrospun TiO_2-graphene composite nanofibers as a highly durable insertion anode for lithium ion batteries. *J. Phys. Chem. C* **116**, 14780–14788 (2012).
24. Mo, R. W., Lei, Z. Y., Sun, K. N. & Rooney, D. Facile synthesis of anatase TiO_2 quantum- dot/graphene nanosheet composites with enhanced electrochemical performance for lithium-ion batteries. *Adv. Mater.* **26**, 2084–2088 (2014).
25. Wang, D. H. *et al.* Self-assembled TiO_2-graphene hybrid nanostructures for enhanced Li-ion insertion. *ACS Nano* **3**, 907–914 (2009).
26. Qiu, B., Xing, M. & Zhang, J. Mesoporous TiO_2 nanocrystals grown *in situ* on graphene aerogels for high photocatalysis and lithium-ion batteries. *J. Am. Chem. Soc.* **136**, 5852–5855 (2014).
27. Yang, S. *et al.* Fabrication of cobalt and cobalt oxide/graphene composites: towards high-performance anode materials for lithium ion batteries. *ChemSusChem* **3**, 236–239 (2010).
28. Yoo, E. *et al.* Large reversible Li storage of graphene nanosheet families for use in rechargeable lithium ion batteries. *Nano Letters* **8**, 2277–2282 (2008).
29. Yang, S., Feng, X., Ivanovici, S. & Müllen, K. Fabrication of graphene-encapsulated oxide nanoparticles: towards high-performance anode materials for lithium storage. *Angew. Chem. Int. Ed.* **49**, 8408–8411 (2010).
30. Park, K. S. *et al.* Long-term, high-rate lithium storage capabilities of TiO_2 nanostructured electrodes using 3D self-supported indium tin oxide conducting nanowire arrays. *Energy Environ. Sci.* **4**, 1796–1801 (2011).
31. Qu, G., Geng, H., Guo, J., Zheng, J. & Gu, H. Facile synthesis of Ag nanowires/mesoporous TiO_2 core-shell nanocables with improved properties for lithium storage. *New J. Chem.* **39**, 7889–7894 (2015).
32. Kim, J. W., Augustyn, V. & Dunn, B. The effect of crystallinity on the rapid pseudocapacitive response of Nb_2O_5. *Adv. Energy Mater.* **2**, 141–148 (2012).
33. Augustyn, V. *et al.* High-rate electrochemical energy storage through Li^+ intercalation pseudocapacitance. *Nat Mater.* **12**, 518–522 (2013).
34. Lubimtsev, A. A., Kent, P. R. C., Sumpter, B. G. & Ganesh, P. Understanding the origin of high-rate intercalation pseudocapacitance in Nb_2O_5 crystals. *J. Mater. Chem. A* **1**, 14951–14956 (2013).
35. Lim, E. *et al.* Facile synthesis of $Nb_2O_5@carbon$ core-shell nanocrystals with controlled crystalline structure for high-power anodes in hybrid supercapacitors. *ACS Nano* **9**, 7497–7505 (2015).
36. Liu, M. N., Yan, C. & Zhang, Y. G. Fabrication of Nb_2O_5 nanosheets for high-rate lithium ion storage applications. *Sci Rep* **5**, 6 (2016).

37. Kim, G. *et al.* TiO₂ nanodisks designed for Li-ion batteries: a novel strategy for obtaining an ultrathin and high surface area anode material at the ice interface. *Energy Environ. Sci.* **6**, 2932–2938 (2013).
38. Rahman, M. M. *et al.* A vein-like nanoporous network of Nb₂O₅ with a higher lithium intercalation discharge cut-off voltage. *J. Mater. Chem. A* **1**, 11019–11025 (2013).
39. Shen, L. *et al.* Three-dimensional coherent titania–mesoporous carbon nanocomposite and its lithium-ion storage properties. *ACS Appl. Mater. Interfaces* **4**, 2985–2992 (2012).

Acknowledgements

Author Contributions

Y.B.L. and M.D.W. proposed and designed the experiments. Y.B.L. and L.W.L. carried out the synthetic experiments and conducted the characterization. Y.B.L. and W.F.Z. performed the HRTEM, SEM characterization and structural analysis. Y.B.L. and M.D.W. analysed the data. Y.B.L. and M.D.W. wrote the manuscript. All the authors participated in discussions of the research.

Additional Information

Supplementary information accompanies this paper at doi:10.1038/s41598-017-07562-5

Competing Interests: The authors declare that they have no competing interests.

Publisher's note: Springer Nature remains neutral with regard to jurisdictional claims in published maps and institutional affiliations.